Comparison of Four Scatter Correction Methods Using Monte Carlo Simulated Source Distributions

Michael Ljungberg, Michael A. King, George J. Hademenos and Sven-Erik Strand

University of Lund, Lund, Sweden and University of Massachusetts Medical Center, Worcester, Massachusetts

Scatter correction in SPECT is important for improving image quality, boundary detection and the quantification of activity in different regions. This paper presents a comparison of four scatter correction methods, three using more than one energy window and one convolution-subtraction correction method using spatial variant scatter line-spread functions. **Methods:** The comparison is based on Monte Carlo simulated data for point sources on- and off-axis, hot and cold spheres of different diameters, and a clinically realistic source distribution simulating brain imaging. All studies were made for a uniform cylindrical water phantom. Since the nature of the detected photon is known with Monte Carlo simulation, separate images of primary and scattered photons can be recorded. These can then be compared with estimated scatter and primary images obtained from the different scatter correction methods. The criteria for comparison were the normalized mean square error, scatter fraction, % recovery and image contrast. **Results:** All correction methods significantly improved image quality and quantification compared to those obtained with no correction. Quantitatively, no single method was observed to be the best by all criteria for all the source distributions. Three of the methods were observed to perform the best by at least one of the criteria for one of the source distributions. For brain imaging, the differences between all the methods were much less than the difference between them and no correction at all. **Conclusion:** It is concluded that performing scatter correction is essential for accurate quantification, and that all four methods yield a good, but not perfect, scatter correction. Since it is hard to distinguish the methods consistently in terms of their performance, it may be that the choice should be made on the basis of ease of implementation.

Key Words: scatter correction; SPECT; brain imaging; Monte Carlo simulated data

$\mathbf{T}$he major physical effects which limit one's ability to accurately quantitate the activity distribution obtained by single-photon emission computed tomography (SPECT) are the photon attenuation in the object, the contribution of

scatter in the image, and the detector response blur. Photon attenuation decreases the number of photons detected by photo-absorption or scattering in the object. Scatter events in the image are caused by photons that are emitted in other directions but scattered in the object into a direction detectable by the SPECT camera. These photons thus carry misleading information regarding the decay location. Detector blurring is caused by the intrinsic spatial resolution of the camera and the inherent design of the collimator.
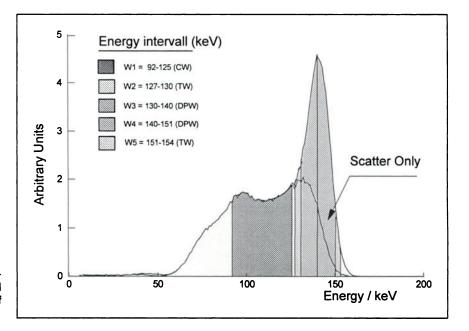
The presence of scatter in the images limits the accuracy of quantification of activity. It does not produce major artifacts comparable to attenuation but reduces image contrast by including a low-frequency blur in the image. The impact of scatter generally depends on the photon energy, camera energy resolution, energy window settings, object shape and the source distribution. Many of these parameters are nonstationary which implies a potential difficulty when developing proper scatter and attenuation correction techniques. However, scatter correction remains essential, not only for quantification, but also for lesion detection and image segmentation. For the latter case, if the boundary of an activity region is distorted by scatter events then the accuracy in the calculated volume will be affected.

A number of scatter correction techniques have been proposed by several investigators (1–12). Among these are methods based on different types of scatter functions in convolution-subtraction techniques (spatial domain methods) and methods that estimate scatter by acquiring events in additional energy windows (energy domain methods).

A major problem when evaluating different correction techniques for attenuation and scatter is validation of the results. Experimental measurements of scatter fractions and response functions are feasible only for simple source and phantom geometries. In these cases, a point source can be measured both in a scattering medium and in air. Scatter images can be calculated by subtraction after first applying narrow-beam attenuation on the air measurement (13). However, problems arise when investigating extended source distributions such as spheres of different diameters. Here, self-absorption and scattering within the spheres can be significant when imaging these sources in air. The complexity increases further when extending to clinically realistic source distributions. It is the performance of the scat-

FIGURE 1. Definition of the energy window settings W_1–W_5 overlaid on a simulated energy spectrum. Note the indication of scatter events in the spectra.

ter correction methods for clinical source distributions which is of interest; measurements in simple phantoms may not represent the performance of the methods with realistic distributions.

The use of Monte Carlo calculations to validate correction methods has been shown to be a successful way to overcome this problem since this evaluation method allows separation of primary and scattered photons into different projection sets. Furthermore, scatter images can, in principle, be calculated for any arbitrary source distribution. Simulated realistic SPECT images (including both primary and scatter) can be corrected for attenuation and scatter and compared to scatter- and attenuation-free ideal images. The accuracy in correction methods can thus be evaluated in an unbiased way since systematic errors can be controlled.

Previously reported Monte Carlo validations of scatter and attenuation correction methods and related parameters have often been made by using simple source distributions and phantom geometries (7,13–15). In addition to these evaluations, there is a need to also investigate more clinically realistic sources to validate and compare correction methods. The aim of this work is to provide such an evaluation by comparing four previously reported scatter correction techniques using Monte Carlo simulated data of a digital brain phantom. Evaluations have also been made for point sources and spheres to characterize the differences between the methods for more standard geometries and allow determination of whether performance in the standard geometry predicts performance in the clinically realistic source distribution.

MATERIAL AND METHODS

Scatter Correction

The scatter correction methods evaluated in this work are individually described below and referred to in the following text

by their abbreviations. The location of each energy window used in this study is denoted W_1–W_5 and shown in Figure 1.

Compton Window Method. The Compton window (CW) method, proposed by Jaszczak et al. (7), is based on acquisition in a secondary energy window (W_1) positioned in the Compton region of the energy pulse-height distribution. In the original work, the upper and lower energy thresholds were held to 125 and 92 keV, respectively, for ^{99m}Tc photons. The acquired scatter was then assumed to be qualitatively equal to the scatter in the photopeak window ($W_3 + W_4$) with respect to the spatial distribution but differ quantitatively by a factor k. The k factor was determined by the ratio between the scatter in the photopeak window and the counts in the secondary energy window. Projections representing scattered photons only are calculated from the equation:

$$P^I_{scatt}(\theta, r) = k \cdot P_1(\theta, r), \qquad \text{Eq. 1}$$

where P_1 denotes the projection acquired in the secondary energy window W_1, θ denotes the projection angle and r denotes the ray in the projection set corresponding to a certain slice of the object. The generally accepted k-value of 0.5 was used in this work. This value was derived from experimental studies of a line source and a 6-cm sphere (7).

Dual Photopeak Window Method. The dual photopeak window scatter correction technique (DPW) is based on acquisition of events in two abutted nonoverlapping energy windows (W_3 and W_4) that are symmetrically located around the photopeak energy (8,9). The lower energy window counts represent photons scattered more than those in the upper window since scatter results in a decrease in the energy carried by the photons. It is assumed that the scatter fraction (SF, e.g., the ratio between the number of scattered events-to-the number of primary events) at each pixel can be estimated from some analytical function of the count ratio between the lower and the upper window, $Rat = P_3(\theta, r)/P_4(\theta, r)$. In the works previously referenced, a power relation was used. However, in this work we have used a third-order polynomial of the form:

$$SF(\theta, r) = A + B \cdot Rat + C \cdot Rat^2 + D \cdot Rat^3. \qquad \text{Eq. 2}$$

The polynomial coefficients A, B, C and D may be obtained from Monte Carlo simulations or from experimental measurement of point sources in different depths in a water phantom. The photopeak scatter projection is finally obtained on a pixel-by-pixel basis by the relation:

$$P_{scatt}^{II}(\theta, r) = P_{3+4}(\theta, r) \cdot \left[\frac{SF(\theta, r)}{1 + SF(\theta, r)} \right], \quad \text{Eq. 3}$$

where the term on the right within the square brackets identifies the scatter-to-total ratio, ST.

Three Window Method. The three window (TW) method, reported by Ogawa et al. (10), uses three energy windows. The first is the ordinary photopeak window and the other two, W_2 and W_5, are two narrow-energy windows located on each side of the photopeak window. The scatter events in the photopeak window are estimated by averaging the projections from the two additional energy windows while taking the different photopeak window size ($W_3 + W_4$) into consideration, according to:

$$P_{scatt}^{III}(\theta, r) = \left[\frac{P_2(\theta, r)}{W_2} + \frac{P_5(\theta, r)}{W_5} \right] \cdot \frac{(W_3 + W_4)}{2}. \quad \text{Eq. 4}$$

In a recent paper by Ogawa et al. (16) the method above has been modified in that only the lower scatter window is used, which is equivalent to setting $P_5(\theta, r)$ equal to zero in Equation 4. It should be noted that this is equivalent to using a smaller Compton window, normalization for window width and a k of 0.5 with the CW method. The two different methods are denoted TW(1) when including the events in W_5 and TW(2) when events in W_5 are not used.

Scatter Line-Spread Function Method. The scatter line-spread function (SLSF) method is a convolution-subtraction technique that uses spatial variant scatter line-spread functions in the modeling of the scatter component (11,12). A knowledge of the source distribution is necessary to select appropriate scatter functions. This information is obtained from reconstructed SPECT images since each voxel is an estimate of the given voxel in the object. It is therefore assumed that the content in each pixel in a SPECT image reflects the amount of activity within the corresponding voxel in the object. This method estimates the scatter contribution from each voxel location in the object by modeling the scatter function for that voxel location. The scatter function is obtained by bilinear interpolation of precalculated scatter line-spread functions. The estimate of the scatter distribution for each voxel to the overall scatter component in the projection data is calculated by a convolution procedure according to:

$$P_{scatt}^{IV}(\theta, r) = \sum_{\gamma(\theta, r)} ST(l) \cdot \sum E_{\gamma(\theta, r)}(i, j) SLSF(l, r - \tau),$$

$$\text{Eq. 5}$$

where ST(l) is the scatter-to-total fraction for a location l; SLSF (l, r) is the scatter line-spread function normalized to unity area; E (i, j) is the SPECT image; γ is the current ray-of-view and τ is a convolution variable.

Attenuation Correction

Correction for attenuation is made by calculating individual correction factors from the reconstructed SPECT images by a reprojection method (17–20). The density distribution of the object and the body outline are taken into account by using density maps so that the correction method may also include nonuniform attenuation. The estimated scatter is subtracted from the uncor-

rected photopeak projection and the result is corrected for attenuation, according to:

$$P_{corr}(\theta, r) = [P_{peak}(\theta, r) - P_{scatt}(\theta, r)] \cdot \left[\frac{P'_{unatt}(\theta, r)}{P'_{att}(\theta, r)} \right], \quad \text{Eq. 6}$$

where P'_{unatt} and P'_{att} are two unattenuated and attenuated projections calculated from the SPECT image. The first reprojection represents the unattenuated case and has been calculated from the line integral of pixels in the emission image along the ray-of-view. The second reprojection is attenuated by calculating the exponential of the attenuation coefficients times the distance between the current pixel and the body outline along the ray-of-view. These attenuated counts are then summed along the ray to yield the count in the projection. The ratio between these two projections is thus the attenuation correction factor. The "good-geometry" linear attenuation coefficient is used since a scatter estimate has been subtracted from the projection data before the attenuation correction is performed.

The Simulated SPECT System

The simulated SPECT system was based on a commercial system (PRISM-3000, Picker International, Bedford, OH) with a low-energy, ultra-high resolution collimator. The thickness of the NaI(Tl) crystal was 0.95 cm and the crystal measured 30.5 × 40.5 cm. The system spatial resolution for SPECT was 0.9 cm FWHM at a distance of 15 cm. The energy resolution and intrinsic spatial resolution were 9.4% (FWHM) and 0.28 cm, respectively, at 140 keV. SPECT projections (64 × 64 matrix mode) corresponding to five different energy windows were calculated during each simulation run. The energy settings for each window (W_1–W_5) are shown in Figure 1. The sum of the two projections acquired in windows W_3 and W_4 was used to create the photopeak SPECT image. The pixel size measured 0.4 × 0.4 cm². SPECT projections were simulated for 64 equidistant views in a 360° rotation mode. The radius of rotation was kept at 13.5 cm for all simulations.

Simulation and Evaluation

Photons of 140 keV were simulated to mimic SPECT studies of ^{99m}Tc. The simulations included the effects of attenuation, scatter and distance-dependent system spatial resolution. Simulation of projections was also made for the ideal case where no scatter or attenuation were included. Ideal case simulations were created to serve as reference studies since these projections only include collimator blur and reconstruction effects. Thus, these reconstructed images should be regarded as ideal images. SPECT projections were simulated from the following source distributions.

Point Source Simulation. Planar simulations of point sources located at multiple depths along the center line of a 20.8-cm phantom were made to calculate the window ratios and corresponding scatter fractions in order to evaluate the polynomial coefficients A, B, C and D in Equation 2 for the DPW method. Two SPECT simulations were also conducted with a point source located in the center of the phantom and 6 cm off-axis in a cylindrical water phantom (length 17 cm, diameter 20.8 cm). These simulations of a simple and well-defined source geometry were made to evaluate estimated scatter point-spread functions from the four scatter correction methods.

Sphere Simulation. Both hot and cold spheres of different radii were simulated in the cylindrical phantom with a specified fraction of simulated activity appearing as background. The spheres were placed symmetrically at a radial distance of 5.8 cm from the axis
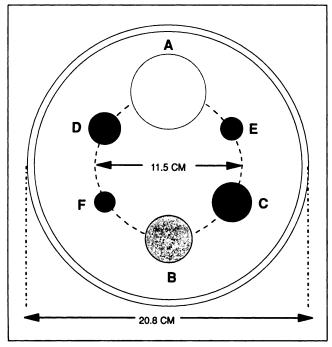
FIGURE 2. Dimensions of the cylindrical water phantom and the size and location of the different simulated spheres.

of rotation, as indicated in Figure 2. The radii for spheres A–F were 3, 2, 1.6, 1.3, 0.9 and 0.8 cm, respectively. The relative activity concentrations were 1 for spheres A and B, 2 for spheres C and D, and 3 for spheres E and F.

Brain Simulation. Our Monte Carlo program (*21*) takes advantage of integer matrices to simulate complicated and realistic source distributions in addition to standard source and phantom geometries. Decays are simulated by calculating the location in the phantom for the apparent position of each of the map cells. The number of decays from the location in the phantom is then given by the content in the corresponding cell in the source distribution matrices. The mathematical source distribution (*22*) of the Hoffman three-dimensional brain phantom (*23*) consists of 19 binary bitmaps and is used to simulate a normal blood flow in the brain. The specific activities of the gray matter, white matter and ventricles are 4:1:0, respectively. The original bitmaps were created in a 256 × 256 matrix mode but were converted to 64 × 64 matrix mode to be readable by our Monte Carlo code. The pixel size of these bitmaps was 0.4 cm and the slice thickness was 0.84 cm. The source distribution was simulated in a cylindrical (20.8 cm diam × 17.5 cm) water phantom.

Each simulated SPECT projection was pre-filtered by a two-dimensional Butterworth filter before image reconstruction. Estimated primary and scatter projections were filtered with a third-order filter with a cut-off frequency of $0.35 \ cm^{-1}$.

The filtered projections were reconstructed to transverse SPECT images (two pixels in thickness) by filtered backprojection using a modified ramp filter (*24,25*). Opposite projection data were averaged by arithmetical mean during the reconstruction process. The attenuation correction was applied using a linear attenuation coefficient of $0.154 \ cm^{-1}$. To reduce the noise enhancement in the corrected projection data after attenuation correction, the corrected projections were, instead of a ramp filter only, reconstructed by using a third-order Butterworth filter order with cut-off equal to $0.4 \ cm^{-1}$.

Scatter point-spread functions (SPSF) for point sources at the center and 6 cm off-axis were obtained from estimated scatter images and evaluated by calculating the difference between "true" SPSFs and estimated SPSFs. The scatter fractions (the ratio of scatter counts-to-primary counts) were calculated from the estimated SPSF images by two circular regions of interests (ROIs). The first ROI covered an area corresponding to the whole phantom. The second ROI was smaller and covered only the point source where the primary counts dominated the response.

The sphere and brain simulations were evaluated by calculating the normalized mean-square error (NMSE), the activity recovery, and the image contrast, all expressed as percentages. Circular ROIs were defined over each sphere in the sphere simulation in such a way that the image of the sources was completely covered. The percentage NMSE was calculated to evaluate the accuracy in the different ROIs in a corrected image, E(i, j), as compared to the ideal simulated image, $E_0(i, j)$ by:

$$NMSE_{ROI} = \frac{\sum \sum [E_0(i, j) - E(i, j)]^2}{\sum \sum E_0^2(i, j)} \cdot 100\%. \quad Eq. \ 7$$

Events within each of the ROIs were integrated for both ideal images and scatter- and attenuation-corrected images. The activity recovery, defined as the percentage ratio of events in a ROI in the corrected images-to-events in the same ROI in the ideal images, were calculated according to:

$$Recovery = \frac{N_{ROI}^{corrected}}{N_{ROI}^{ideal}} \cdot 100\%, \quad Eq. \ 8$$

where N_{ROI} is the count density in the ROI. The image contrast was calculated from ROIs defined in each of the cold regions and a background ROI, defined in the center of the phantom, by:

$$Contrast = \left[1 - \frac{N_{ROI}}{N_{BG}}\right] \cdot 100\%, \quad Eq. \ 9$$

where N_{ROI} and N_{BG} are count densities for the sphere ROI and for the background ROI, respectively. The brain simulation was evaluated by calculating the activity recovery and NMSE for six irregular ROIs over structures that are important in neurophysiology. The image slice used for calculating the ROIs was the one that included the basal ganglia. The image contrast was not calculated for this phantom type since the contrast is not consistently defined in a heterogeneous activity distribution.

RESULTS AND DISCUSSION

Point Source Simulation

The coefficients A, B, C and D for the polynomial used in the DPW method were −3.834, 7.822, −5.4057 and 1.415, respectively, and were used both for the point sources and for the extended sources. Figure 3 shows profiles of the true reconstructed SPSF minus reconstructed SPSFs which were estimated by the four scatter correction methods. A flat profile of zero counts would represent a perfect scatter estimate. It can be seen that the scatter close to the source location is underestimated for the CW method since we get a positive peak. This is due to the different spatial distribution of counts when acquiring in a lower energy window as opposed to the photopeak window (*26*). The DPW method provides the best estimate
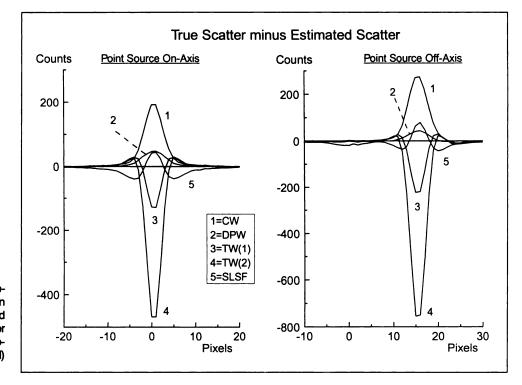
FIGURE 3. Profiles representing the difference between true reconstructed scatter and estimated reconstructed scatter obtained for a point source located in the center (left panel) and 6 cm off-axis (right panel).

of scatter for the two point sources although a small underestimation can be seen close to the source location for the center location and for the off-axis source location. For DPW there is no significant difference in predicting the scatter estimate as a function of source location. The TW(2) method significantly overestimates the scatter very close to the source location and especially when the source is off-axis. This is most likely due to the use of the third window on the high energy side of the photopeak when estimating scatter. It can be seen that if the higher window is not used (shown as the curve labeled TW(1)), then the overestimation is still present near the source but significantly reduced. As the distance from the source increases, the TW(1) method switches from an overestimate to a small underestimate. The SLSF method underestimates scatter close to the source location but overestimates scatter at distances away from the source. This is significant for both source locations. The reason for this is that in this technique, the scatter is modeled from a reconstructed image of the point source distribution. Since the SPECT

image is affected by the spatial resolution of the system, the sampled source distribution will not be a well-defined point source but rather a Gaussian blurred source. This will then have an impact on the spatial distribution of scatter estimate.

Table 1 shows calculated scatter fractions from the point source simulations. The TW(2) method significantly overestimates scatter fraction in both ROIs, and especially in the small ROI. The TW(1) method gives the best estimate for both small and large ROIs. From Figure 3, it can be noted that this performance is due to the averaging of over and under corrections within the ROI. The DPW method also gives close estimates of the scatter fraction for both ROIs. The SLSF method estimates the scatter fraction within 20% for small ROIs but significantly overestimates for large ROIs. The CW method underestimates the scatter fraction in both ROI sizes and especially in the small ROI.

Since there was such a significant improvement by not using the upper energy window for the TW method, the

TABLE 1
Estimated Scatter Fractions Obtained for Point Sources Located in Center and Off-axis Compared to True Scatter Fractions*

ROI	CW		DPW		TW(1)		TW(2)		SLSF		True
Center, Large	0.10	−33%	0.12	−20%	0.20	33%	0.13	−13%	0.23	53%	0.15
Center, Small	0.06	−45%	0.09	−18%	0.18	64%	0.11	0%	0.13	18%	0.11
Off-axis, Large	0.09	−18%	0.11	0%	0.19	73%	0.12	9%	0.19	73%	0.11
Off-axis, Small	0.06	−40%	0.09	−10%	0.18	80%	0.11	10%	0.12	20%	0.10

*The percentage deviation from the true scatter fraction is also given. Note that the results are obtained for a single reconstructed slice and not from projection data.
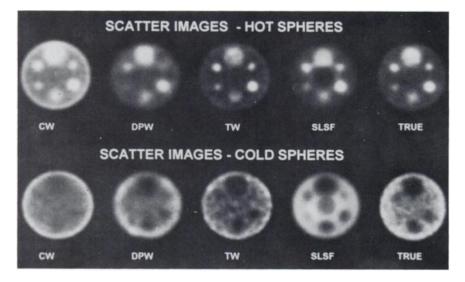
FIGURE 4. Images of reconstructed scatter for hot-sphere (top row) and cold-sphere simulations (bottom row). The images located to the right represent the true reconstructed scatter. The other images show estimated scatter obtained from the different methods.

evaluations of the sphere and the brain simulations were carried out only for the version with only the lower window, i.e., the TW(1) method.

Sphere Simulation

Figure 4 shows reconstructed estimated scatter images and true scatter images for both hot spheres (top row) and cold spheres (bottom row).

Hot Spheres. The scatter obtained from the CW method is very uniformly distributed, as can be seen from Figure 4 (upper row). The method predicts more scatter between the sources than is present in the true scatter image. This is a result of the acquisition of events in the Compton region that result from large-angle scattered photons. The scatter estimate obtained from the DPW method bears a close resemblance to the true scatter even though significant low-frequency noise has been introduced. The TW(1) method gives a good estimate of the scatter distribution even if the scatter image looks somewhat "sharper" than the true scatter image. This might result when some of the primary photons are included in the lower energy window due to the limited energy resolution of NaI(Tl). The SLSF method also gives a good estimate of the scatter but tends to underestimate scatter close to the center of the phantom. Also, it can be seen that scatter between the sources

has been overestimated. The reasons for these effects are not yet understood.

Table 2 shows the percentage activity recovery and NMSE for the counts obtained in the ROIs defined over the hot spheres. All methods result in a recovery that is within 2% of 100%. The standard deviation of the activity recovery is, however, somewhat higher for the DPW method. The average in NMSE is nearly the same in magnitude for all correction methods but the standard deviation indicates a large spread for the CW and the DPW methods.

Cold Spheres. Figure 4 (lower row) shows that the scatter estimate from the CW method is very uniformly distributed. Only the two largest cold spheres can clearly be seen. The DPW and the SLSF method give about the same scatter estimate although the SLSF method results in a much smoother scatter image. The same lower scatter estimate close to the center appears in the SLSF image as for the hot sphere case. When comparing scatter obtained from the TW(1) method with the true scatter image, it can be seen that the former gives a very good scatter estimate but with somewhat sharper edges of the cold-spheres than is the case for the true scatter image.

Table 3 shows the percentage contrast for the cold

TABLE 2
Results from Evaluation of the Hot Spheres in the Cylindrical Water Phantom

Sphere	Recovery (%)				NMSE (%)			
	CW	DPW	TW(1)	SLSF	CW	DPW	TW(1)	SLSF
A	99	99	102	100	0.1	0.1	0.1	0.2
B	95	97	98	97	0.3	0.2	0.2	0.2
C	98	98	98	96	0.2	0.2	0.2	0.2
D	101	104	103	101	0.5	0.7	0.4	0.4
E	96	100	99	98	1.4	1.4	1.0	0.9
F	101	106	104	104	0.9	1.3	0.9	0.9
Average	98.3	100.7	100.7	99.3	0.6	0.7	0.5	0.5
s.d.	2.3	3.2	2.4	2.7	0.5	0.5	0.4	0.3

TABLE 3

TABLE 3
Results from Evaluation of the Cold Spheres in the Cylindrical Water Phantom

Sphere	Image contrast (%)					
	CW	DPW	TW(1)	SLSF	IDEAL	UNC*
A	100	99	98	100	96	91
B	97	94	92	95	90	80
C	98	94	90	94	88	77
D	79	71	64	74	64	53
E	41	36	35	45	32	18
F	28	28	24	36	25	9
Average	73.8	70.3	67.2	74.0	65.8	54.7

*Unc is an abbreviation for uncorrected

sphere case. By the column averages, it can be seen that the TW(1) method predicts the contrast very accurately as compared to the average contrast in the ideal image. The other methods, on average, overcorrect for the presence of scatter. For the CW method, this can be explained by large-angle photon scattering in the object resulting in scatter events far away from the source. In this case, the scatter estimate will overestimate the true scatter content. For the SLSF method, the effect can be a result of inaccurate scatter modeling since the reconstructed SPECT image used is not a perfect image of the true source distribution. This may have an effect when quantifying regions in the image that are close to areas of high activity.
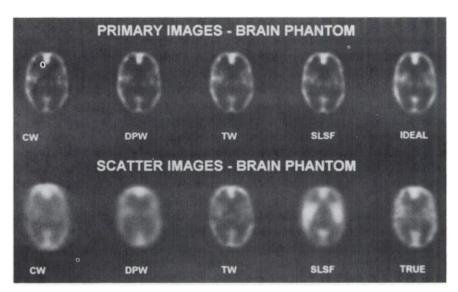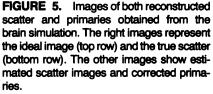
Brain Simulation

Figure 5 shows reconstructed corrected primary images (top row) and scatter images (bottom row) obtained from the brain simulation. It is hard to judge any major differences in the corrected primary images. The effect of the large-angle scatter in the Compton window acquisition (W_1) can be clearly seen in the scatter image estimated by the CW method. Scatter is present in areas where no activity is simulated (left and right parts of the image). The

scatter estimates from the DPW and the SLSF method agree best with the true scatter image even though low frequency noise can be seen in the DPW image.

Table 4 shows the percentage activity recovery and percentage NMSE for the six irregular ROIs which cover important structures of the brain. The DPW and SLSF methods here give very good activity recovery values which average within 2%. CW tends to undercorrect and TW(1) overcorrects. The NMSE values are best for the SLSF and DPW methods, and slightly worse for the CW and TW(1) methods. All methods result in a significant improvement compared to no correction.

On the basis of both Monte Carlo calculation and experimental measurements of point sources, a value of k equal to 0.5 has been widely accepted in the literature for the CW method and has also been used in this work. The general idea of the technique is to find a k that scales the amount of scatter in the second energy window to the amount of scatter in the photopeak energy window. However, due to the depth-dependence of scatter, the value of k is unique for each source location and object size in addition to other camera-specific parameters (26). Thus, the value of k may

FIGURE 5. Images of both reconstructed scatter and primaries obtained from the brain simulation. The right images represent the ideal image (top row) and the true scatter (bottom row). The other images show estimated scatter images and corrected primaries.

TABLE 4
Percentage Recovery and NMSE Calculated in Different Clinical Structures in the Hoffman Three-Dimensional Brain Phantom

Structure	Recovery (%)						NMSE (%)				
	CW	DPW	TW(1)	SLSF	NSA	NSNA	CW	DPW	TW(1)	SLSF	NSA
Left basal ganglia	94	97	102	98	129	30	1.5	1.3	1.3	1.0	8.8
Right basal ganglia	94	97	101	98	129	30	1.4	1.1	1.1	1.0	8.8
Left frontal cortex	98	103	105	100	125	42	0.7	0.7	0.9	0.5	6.7
Medial frontal cortex	101	104	106	100	125	40	1.0	1.1	1.3	0.7	7.0
Right frontal cortex	98	103	105	98	125	40	0.6	0.6	0.8	0.5	6.4
Posterior medial cortex	97	101	103	99	121	42	0.7	0.5	0.7	0.4	5.0
Average	97.0	100.8	103.7	98.8	125.7	37.3	0.98	0.88	1.02	0.68	7.12
s.d.	2.4	2.9	1.8	0.9	2.7	5.2	0.35	0.30	0.23	0.24	1.34

NSNA = no scatter and attenuation correction; NSA = attenuation-corrected but no scatter-corrected data.

have to be determined from simulations of a point source in the center of a cylindrical water phantom, as has been described in the work by Jaszczak (27), for the camera, attenuator parameters and energy window settings used. The k value for the CW method determined in this way for this camera system was calculated to be 0.38. However, when this k value is used, the scatter fraction for the source locations and ROIs in Table 1 was found to be 0.08, 0.04, 0.05 and 0.06, respectively, with relative errors of −47%, −64%, −57% and −50%. The significant underestimate for point sources with this method was not observed for the extended source distributions (Tables 2 and 3). Since k varies with depth for point sources (26), it may be that this variation is averaged out for extended sources imaged over 360°. Still, one may need to carefully obtain a k value for each SPECT system, window setting and, if possible, for different object sizes and source distributions.

It is also interesting to note that the performance of the correction methods for point sources did not always predict the performance of the methods for an extended clinical source distribution. For example, the SLSF method did not perform as well as the TW(1) method for point sources, but performed better for the brain simulation. Also the CW method performed poorly for the point sources, but was much improved with the extended source where under- and overestimates could average out. It is therefore important to perform a test of scatter correction methods for source distributions which closely match the clinical application to which they will be applied. The Monte Carlo simulation is a useful tool for performing such a test.

CONCLUSION

A comparison of four different scatter correction techniques has been made from Monte Carlo simulated SPECT projections of point sources, spheres of different diameters and a clinically realistic source distribution of the brain perfusion.

CW Method. Determination of a value for k is a problem for the CW method. As discussed above, a k value of 0.5 is commonly used but this may vary with the imaging situa-

tion. Based on this study, a value of 0.5 for k for brain imaging and the energy windows used seems to be a reasonable choice. Once k is defined, this method does have the advantage of being very easy to implement and use clinically.

DPW Method. When comparing quantitative data, the DPW method gave the best performance for point sources (when the over- and under-correction of TW(1) are taken into account), but was not consistently better than the other methods for the extended source distributions. DPW's sensitivity to image noise and the improved performance of the other methods for estimating scatter with extended sources are responsible for this change. DPW requires the determination of the coefficients used in the regression relationship of Equation 2, and that the windows be reproducibly positioned thereafter. It is thus harder to implement than the CW and TW(1) methods. For a pair of windows split at the emission energy of the photon, DPW also has a problem with stability of the regression relation over time and location on the face of the camera (28).

TW Method. The TW method is the easiest method to implement since it requires no system-specific calibration. However, the use of the window above the photopeak is questionable for ^{99m}Tc; without the upper window the number of counts in the narrow lower window might make the method sensitive to noise. This work shows that neglecting the upper window improves performance.

SLSF Method. The SLSF method is much more complicated than the other three methods and may be difficult to implement on a routine basis since accurate scatter functions need to be available. In this work, scatter functions have been calculated from Monte Carlo simulations. Work is, however, ongoing in simplifying this by applying the methods of Frey et al. (29).

A general disadvantage for window correction methods is that some commercial systems do not include the option of acquiring events in separate windows to separate studies. Also, further problems may arise if one needs to acquire events in the lower Compton region for accurate boundary detection in the attenuation correction, therefore

requiring a different window than that of the scatter correction method. Here, the SLSF method has an advantage since it is an analytical method applied on photopeak data. The event acquired by the CW method can also be used for boundary detection due to the location of this secondary energy window.

All correction methods significantly improved the image contrast. Generally, it was shown that the differences in the estimated scatter distributions did not have a significant impact on the final quantitative results since most recovery calculations were found to be within $\pm 5\%$. It may be concluded that in modern cameras with good energy resolution, the impact of scatter is reduced since a narrower energy window can be used (15% in this study). The results also indicate that the differences in performance between different types of scatter correction techniques are minimal for ^{99m}Tc brain perfusion imaging. Thus, a user may select a correction method that is easy to implement on a particular system. These conclusions are true only for a brain-sized attenuator. With a larger attenuator (such as the abdomen) more scatter will be produced and larger effects due to scatter would therefore be expected.

ACKNOWLEDGMENTS

REFERENCES

1. Axelsson B, Msaki P, Israelsson A. Subtraction of Compton-scattered photons in single-photon emission computed tomography. *J Nucl Med* 1984;25:490–494.
2. Egbert SD, May RS. An integral-transport method for Compton-scatter correction in emission computed tomography. *IEEE Trans Nucl Sci* 1980; 27:543–548.
3. Gilardi MC, Bettinardi V, Todd-Prokopek A. Assessment and comparison of three scatter correction techniques in single photon emission computed tomography. *J Nucl Med* 1988;29:1971–1979.
4. Koral KF, Clinthorne NH, Rogers WL. Improving emission computed tomography quantification by Compton scatter rejection through offset windows. *Nucl Inst Meth Phys Res* 1986;A242:610–614.
5. Koral KF, Wang X, Rogers LW. SPECT Compton scattering correction by analysis of energy spectra. *J Nucl Med* 1988;29:195–202.
6. Msaki P, Axelsson B, Dahl CM. Generalized scatter correction in SPECT using point scatter distribution functions. *J Nucl Med* 1987;28:1861–1869.
7. Jaszczak RJ, Greer KL, Floyd CE, Harris CC, Coleman RE. Improved SPECT quantification using compensation for scattered photons. *J Nucl Med* 1984;25:893–900.
8. King MA, Hademenos GJ, Glick SJ. A dual photopeak window method for scatter correction. *J Nucl Med* 1992;33:605–613.
9. Hademenos GJ, Ljungberg M, King MA, Glick SJ. A Monte Carlo investigation of the dual photopeak window scatter correction method. *IEEE Trans Nucl Sci* 1993;40:179–185.
10. Ogawa K, Harata H, Ichihara T, Kubo A, Hashimoto S. A practical method for position dependent Compton-scatter correction in single photon emission CT. *IEEE Trans Med Imag* 1991;10:408–412.
11. Ljungberg M, Strand S-E. Scatter and attenuation correction in SPECT using density maps and Monte Carlo simulated scatter functions. *J Nucl Med* 1990;31:1559–1567.
12. Ljungberg M, Strand S-E. Attenuation and scatter correction in SPECT for sources in a nonhomogeneous object: a Monte Carlo study. *J Nucl Med* 1991;32:1278–1284.
13. Manglos SH, Floyd CE, Jaszczak RJ, Greer KL, Harris CC, Coleman RE. Experimentally measured scatter fractions and energy spectra as a test of Monte Carlo simulations. *Phys Med Biol* 1987;22:335–343.
14. Floyd CE, Jaszczak RJ, Harris CC, Greer KL, Coleman RE. Monte Carlo evaluation of Compton scattered subtraction in single photon emission computed tomography. *Med Phys* 1985;12:776–778.
15. Beck J, Jaszczak RJ, Coleman RE, Stermer CF, Nolte LW. Analysis of SPECT including scatter and attenuation using sophisticated Monte Carlo modeling methods. *IEEE Trans Nucl Sci* 1982;29:506–511.
16. Ogawa K, Chugo A, Ichihara T, Kubo A, Hashimoto S. Quantitative image-reconstruction using position-dependent scatter correction in single photon emission CT. *Conference record of the 1992 nuclear science symposium and the medical imaging conference*. Orlando: 1993;1011–1013.
17. Murase K, Itoh H, Mogami H, et al. A comparative study of attenuation correction algorithms in single photon emission computed tomography (SPECT). *Eur J Nucl Med* 1987;13:55–62.
18. Axelsson B. Studies of a techniques for attenuation correction in single photon emission computed tomography. *Phys Med Biol* 1987;32:737–749.
19. Ljungberg M, Strand S-E. Attenuation correction in SPECT based on transmission studies and Monte Carlo simulations of build-up functions. *J Nucl Med* 1990;31:493–500.
20. Ljungberg M, King MA, Strand S-E. Quantitative SPECT: verification for sources in an elliptical water phantom. *Eur J Nucl Med* 1992;19:838–844.
21. Ljungberg M, Strand S-E. A Monte Carlo program simulating scintillation camera imaging. *Comp Meth Progr Biomed* 1989;29:257–272.
22. Kim H-E, Zeeberg BR, Fahey FH, Bice AN, Hoffman EJ, Reba RC. Three-dimensional SPECT simulations of a complex mathematical three-dimensional brain model and measurements of the physical three-dimensional brain phantom. *J Nucl Med* 1991;32:1923–1930.
23. Hoffman EJ, Cutler PD, Digby WM, Mazziotta JC. Three-dimensional phantom to simulate cerebral blood flow and metabolic images for PET. *IEEE Trans Nucl Sci* 1990;37:616–620.
24. Glick SJ, King MA, Penney BC. Characterization of the modular transfer function of discrete filtered backprojection. *IEEE Trans Med Imag* 1989;8: 203–213.
25. Rosenfeld A, Kak AC. *Digital picture processing, 2nd edition, volume 1*. New York: Academic Press; 1982.
26. Ljungberg M, Msaki P, Strand S-E. Comparison of dual-window and convolution scatter correction techniques using the Monte Carlo method. *Phys Med Biol* 1990;35:1099–1110.
27. Koral KF, Fayez MS, Buchbinder S, Clinthorne NH, Rogers WL, Tsui BMW. SPECT dual-energy window Compton correction: scatter multiplier required for quantification. *J Nucl Med* 1990;31:90–98.
28. King MA, Hademenos GJ, DeVries DJ, Penney BC, Morgan HT, Jarkewicz CG. Implementation and testing of the dual photopeak window scatter correction method on a multi-headed SPECT system. In: *Conference record on the 1992 IEEE nuclear science symposium and medical imaging conference*. Orlando, FL: IEEE; 1993:1179–1181.
29. Frey EC, Tsui BMW. Parameterization of the scatter response function in SPECT imaging using Monte Carlo simulation. *IEEE Trans Nucl Sci* 1990; 37:1308–1315.